Experimental and numerical investigation binary mixture mass transfer in a gas – Liquid membrane contactor

Valentin Fougerit, Victor Pozzobon, Dominique Pareau, Marc-André Theoleyre, Moncef Stambouli

Journal of Membrane Science DOI: 10.1016/j.memsci.2018.10.042

Experimental and numerical investigation binary mixture mass transfer in a gas – liquid membrane contactor

Valentin Fougerit, Victor Pozzobon, Dominique Pareau, Marc-André Théoleyre, Moncef Stambouli*

LGPM, CentraleSupélec, Université Paris-Saclay, SFR Condorcet FR CNRS 3417, Centre Européen de Biotechnologie et de Bioéconomie (CEBB), chemin des Sohettes 51110 Pomacle, France

*Corresponding author: victor.pozzobon@centralesupelec.fr

1 Abstract

CO_2 removal from binary mixture gaseous streams using hollow fibers membrane module under physical absorption (water) has been investigated. The impact of the gas composition on the mass transfer efficiency was experimentally investigated with a CO_2/CH_4 mixture of varying composition ($y_{CO_2}^{in} = 10 - 90\%$), covering a wide range of process: natural gas sweetening (5-10 % CO_2), post-combustion carbon capture (10-15 % CO_2), for biogas upgrading to biomethane (35-50 % CO_2), ... As expected, the absorbed CO_2 flux is increasing with the CO_2 partial pressure. Yet the absorbed CO_2 flow is multiplied by a factor up to 15 between a 10 and a 90 % inlet CO_2 molar fraction, while applying a factor 9 to the inlet flow parameters. This underlines the existence of a non-trivial behavior.

In the meantime, a 2D numerical model describing the absorption of CO_2 in a binary gas mixture, based on the internal module geometry and on a local description of the hydrodynamics was proposed. Its development showed that in order to capture the key phenomena, a proper description of mass transfer in transition zone (Knudsen number around 0.34) is mandatory. Implementing this description allowed the model to accurately describe mass transfer over a wide range of gas composition and flow rate, without relying on any fitted parameter.

Highlights

- Absorption of a binary gas mixture was modelled in cross-flow HFMMs
- CO_2 absorption ratio is divided by up to a factor 15 in the presence of CH_4
- Resistance-in-series has to be adapted to describe HFMM mass transfer
- Transition zone equations are implemented without fitted parameter
- The model predicts mass transfer over a wide range of gas composition and flow rate

Keywords

Membrane contactor; CO_2 absorption; Gas mixture; Diffusion; Mathematical modeling

2 Introduction

Since its development as a technology for the artificial lung, membrane contactor has risen as a promising mass exchanger device for gas-liquid applications. In use today for carbonation in the beverage industry or for deoxygenation for ultrapure water production, it offers promising perspectives in various fields such natural gas sweetening [1] (5-10 % CO_2), as post-combustion carbon capture (PCC) [2,3] (10-15 % CO_2), biogas upgrading to biomethane [4,5] (35-50 % CO_2) or water desalination [6]. This type of mass exchanger offers a high specific area ($> 1\ 000\ m^2.m^{-3}$) compared to conventional gas-liquid reactors (Figure 1), which paves the way to process intensification.

Thanks to membrane hydrophobic properties, Hollow Fibers Membrane Modules (HFMMs) offer a non-dispersive contact to gas-liquid absorption systems with valuable advantages: operational flexibility (independent control of gas and liquid flowrates and pressures), a known interfacial area supported by the membrane, modularity (linear scale-up and ease of maintenance) and compactness [2,10,11]. Nevertheless, the implementation of membrane contactors technologies at an industrial scale is conditioned by a comprehensive understanding of the mass transfer phenomenon and the development of relevant scale-up methodologies.

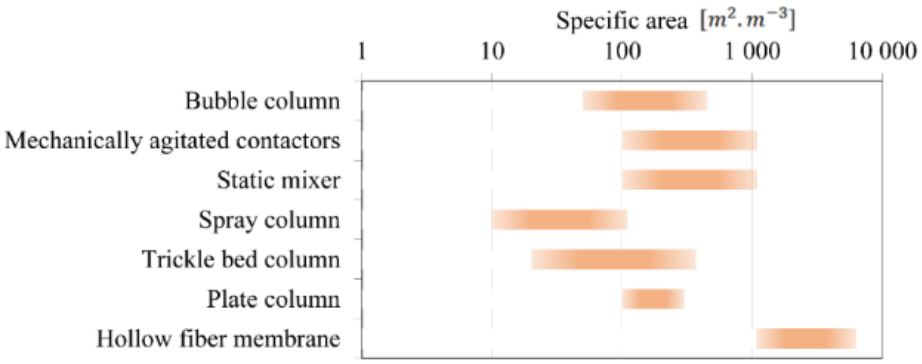

Figure 1 – Specific area of gas-liquid contacting devices (adapted from [7–9])

Indeed nowadays, the CO_2 removal stage of a process is led in classical, high volume equipment such as packed column. In this process, two strategies that may not be driven by the same mass transfer limitations coexist: chemical and physical absorption. The selected strategy is dependent on the application:

- For PCC, which is a promising carbon mitigation process since it can easily be implemented to existing power plants to remove CO_2 at a concentration 4-15% in the gas stream [12], chemical absorption is preferred over physical absorption by the use of amine, amino-acids or promoted carbonate solutions [2,3,13,14]. The high affinity of these reactants with CO_2 allows to selectively react with CO_2 and reduce the size of the equipment. Membrane contactors can bring further intensification to this field both at the absorption and the desorption steps. Indeed, polypropylene (PP) and polytetrafluoroethylene (PTFE) hollow fibers demonstrated a 4-fold increase in the overall mass transfer coefficient ($K_G a$) compared to packed column [15]. Polyvinylidene fluoride (PVDF) membrane was evidenced to be more subject to membrane wetting (and subsequent loss in mass transfer efficiency) than PTFE membranes in the case of monoethanolamine (MEA) and 2-amino-2-methyl-1-propanol (AMP) solutions [16]. Among the amine-solutions, a blend of DEEA/PZ with a molar ratio of 1.50:0.5 demonstrated high absorption and desorption rates in a PTFE HFMM, with a cyclic CO_2 capacity of 0.8540 mol CO2/L [17].
- Membrane contactors may also find a suitable application in CO_2 capture for biogas upgrading to biomethane (35-50 % CO_2 initially), as biogas production units do not necessarily reach a scale large enough to support conventional technologies capital expenditures (CAPEX). A preliminary study demonstrated that chemical absorbent (NaOH) can upgrade over 99% purity while a 85% CH_4 biomethane was produced using a physical absorbent (water) [4]. The investigation of the process configuration and operating conditions allowed to reach a 98% methane content with the same membrane module [18]. In this aim, the effect of operating parameters on CO_2 removal efficiency with reactive potassium arginate (PA) solutions highlighted the the advantage to operate under turbulent conditions thanks to numerical simulations [19]. Regarding mass transfer limitations, the absorbed CO_2 flux in a biogas upgrading to biomethane application is dependent on the liquid velocity for physical absorption while it is controlled by the gas velocity for a chemical system [4]. Under a lower 10 % CO_2 fraction in the gas inlet, another study confirmed that CO_2 physical absorption is driven by the liquid flowrate [20]. In this reactive case, the mass transfer limitation is reported to be in the liquid phase for physical absorbents, due to a lower CO_2 diffusivity in the water than in pure gaseous carbon dioxide ($D^l_{CO_2-water} = 1.78 \times 10^{-9}\ m^2.s^{-1}$ against $D^g_{CO_2} = 1.22 \times 10^{-5}\ m^2.s^{-1}$ under atmospheric pressure at 293 K).

Among the CO_2 absorption experimental studies involving membrane contactors, the liquid and gas flowrates are the main parameters to be investigated, taking sometimes into account pressure and temperature conditions. The development of a mass transfer model for dense membrane contactors (mass transfer is occurring by diffusion in the membrane polymer) indicated that both the membrane and liquid boundary layer were driving the mass transfer [11]. However, regarding porous membrane contactors, very few studies have systematically investigated the impact of the gas phase composition on the mass transfer efficiency since only specific inlet conditions were considered (5-10% CO_2 for natural gas sweetening, 10-15% CO_2 for PCC, 40-50 % CO_2 for biogas upgrading to biomethane). The absorbed CO_2 flux was experimentally found to increase with the CO_2 fraction in the inlet gas using water as the absorbent [21]. For PCC applications, numerical simulations proved that the increase of the CO_2 gas fraction in the range 10-20 %v/v reduces the carbon capture rate in the case of various amine reactive systems due to the saturation of the absorbent at low concentration [22,23]. The rise in the CO_2 partial pressure necessarily enhances the absorbed CO_2 flux. However, the impact on the overall mass transfer coefficient K_L was not investigated. The gas composition may play a role on the mass transfer mechanism, especially in applications with a significant variation in

the gas composition such as biogas upgrading to biomethane (the CO_2 fraction is varying from 40-50% to <3%). For instance, the variation of the gas partial pressures was stated to imply a decrease in the selectivity of the process from 166 to 106 [4]. The comparison of experimental studies for CO_2 absorption in different applications (Table 1) shows that the absorbed CO_2 flux $J_{CO_2}^{abs}$ tends to decrease with a decreasing inlet CO_2 fraction.

Ref.	Conf.	Membrane material	Membrane area s $[m^2]$	Inlet gas composition	P_g $[bar\ g]$	$J_{CO_2}^{abs}$ $[10^{-4}\ mol_{CO_2}.m^{-2}.s^{-1}]$	Comments (for absorption in water)
[24]	Abs.	PP (Membrana)	1.4	Pure CO_2	0	Dry mode: 11 – 24 Wet mode: 9 – 14	$J_{CO_2}^{abs}$ increases with the liquid flowrate
[25]	Abs. Abs./Des.	PP (SepraTek Inc.)	0.25	CO_2/ CH_4 50/50	1.5 – 4.5	2.9 – 3.4	$J_{CO_2}^{abs}$ is increasing with the gas pressure but is almost not impacted by the increase of the liquid flowrate
[26]	Abs./Des	PP (Membrana)	2.8	CO_2/ CH_4 50/50	2 - 6	1.3	Increasing the gas pressure results in a limited $J_{CO_2}^{abs}$ rise, but it decreases the CO_2/ CH_4 selectivity
[4]	Abs.	PP (Membrana)	0.58	CO_2/ CH_4 40/60	NS[1]	0.8 – 1.7	$J_{CO_2}^{abs}$ linearly increases with the liquid flowrate
[27]	Abs.	PP (Membrana)	0.1588	CO_2/N2 25/75	0	< 1.7	Membrane module is used for the characterization of Henry and diffusion coefficients
[28]	Abs.	PP (Membrana)	0.09	CO_2/N_2 20/80	NS	2 – 3	$J_{CO_2}^{abs}$ increases with the liquid velocity No significant effect of the gas flowrate on $J_{CO_2}^{abs}$
[29]	Abs.	ePTFE (Sumitomo) / PFA (Entegris)	0.314 / 0.034	CO_2/H_2S/ CH_4 5/2/93	1 - 50	0.09 – 0.11 / 1.3 - 1.7 (@ 1 bar g)	$J_{CO_2}^{abs}$ is slightly increasing with the gas flowrate $J_{CO_2}^{abs}$ linearly increases with the gas pressure in a moderate pressure range

Table 1 – Absorbed CO_2 flux and effect of operating parameters in various applications involving porous membrane contactors

These discrepant findings suggest a strong need of the scientific community for an unifying modelling approach. In this regard, several authors have addressed the question of mass transfer phenomena in HFMM through numerical modelling. As stated in a previous study [30], 1D and 2D simulations, or even a combination of both, are developed to model gas-liquid mass transfer:

- 1D description along the contactor axis relies on the estimation of mass transfer coefficients in the different phases of the system (gas, membrane, liquid) [16,31,32];
- 2D description of the whole contactor, allowing to describe such configurations such as crow-flows [33–36].

In addition, in order to gain further insights on local mass transfer phenomena, some authors have investigated them at the fiber scale. 2D models are typically used for this kind of approaches. They consider the fiber radial direction to describe mass transfer in the different phases and perform a numeric resolution considering a single fiber [20,27,28,37–41].

The comparison of these two modelling strategies demonstrated that they equally perform for a PCC application [42,43]. Though, they still require the membrane mass transfer coefficient k_m to be a fitting parameter on which the model is highly dependent [35,44,45]. Furthermore, the good performance of the 1D approach for chemical absorption was explained by a relatively flat concentration profile in the liquid phase, which implies a low mass transfer resistance [12]. A higher deviation may appear when considering systems with a low reactivity.

[1] Not Specified (NS)

Nevertheless, the above-mentioned models suffer two weaknesses that impair their capability to provide membranes performances further understanding. First, they are lacking a description of the complex shellside hydrodynamics. For instance, some industrial ranges of HFMM (such as the widely used Liqui-Cel® Extra-Flow commercialized by Celgard) have a central diverting baffle: the addition of mixing points enhances the mass transfer [43]. Second, these models are essentially applicable in the operating condition range the membrane mass transfer coefficient k_m was fitted.

Therefore, the aims of the current paper are: (1) to experimentally investigate the effect of the inlet gas composition and flow rate on the absorbed CO_2 flux and the mass transfer efficiency, thus covering the two regimes highlighted in Table 1, (2) to propose a mechanistic model, without fitted parameter, that could describe mass transfer in HFMM.

3 Material and methods

3.1 Experimental set-up

The experimental set-up (Figure 2) was designed to monitor the CO_2 absorption flux from a CO_2/CH_4 mixture, and the upgrading performances of the membrane module under different operating conditions (flowrates and pressures). The inlet gas flowrate Q_g^{in} and its composition are controlled by a 2-way mixer equipped with mass flow controllers (Bronkhorst In-Flow CTA). Pure gases (CO_2, CH_4 - Air Liquid AlphaGaz 1 standard > 99.95 %v/v) were used to produce synthetic mixtures. After going through the absorption module, the outlet gas flowrate Q_g^{out} is measured in another mass flow controller (Bronkhorst Low-ΔP-Flow). The process gas pressure P_g is regulated with a PID controller connected to the solenoid valve of the outlet mass flow controller. It takes about 5 minutes for the gas flows and pressure to stabilize at their setpoints. Uncertainties related to thermal mass flowmeters are detailed in Table 3.1.

	In-Flow CTA	Low-ΔP-Flow
Range $\left[NL_{N_2}.h^{-1}\right]$	100 - 1000	100 - 1000
Precision	± (1 %RD + 1 %FS[2])	± (1 %FS)
Repeatability	± (0.2 %FS)	± (0.2 %RD)
Calibration uncertainty	± 0.5 %RD	± 0.3 %RD

Table 3.1 – Uncertainties of thermal mass flowmeters

In this open-loop configuration, reverse osmosis (RO) water is flowing counter-currently on the fiber shellside and is discharged after CO_2 removal. Two pumps (Iwaki MDT-20LCA and Iwaki MDG-M4S6B) are respectively regulating the pressure P_l and the flowrate Q_l. They are controlled by a pressure transmitter PT 11 and a vortex flowmeter FI (Liqui-View, precision < ± 2 %RD) through frequency converters. Liquid pH is measured in a flow-through fitting positioned after CO_2 absorption step (Mettler-Toledo InPro 4262i). Water temperature is regulated at $21 \pm 0.5°C$ with a cryostat through a plate heat exchanger (AlfaLaval).

Gas composition analysis at the gas inlet and outlet are performed with a micro Gas Chromatography (Agilent 490) equipped with 2 columns (10m Molsieve 5Å and 10m PoraPLOT U). It is combined with a selection valve (VICI 6-streams selector valve). The pressure of the samples were reduced to 200 mbar g by pressure reducing controllers. Analysis are performed twice to ensure reliable results. The process is evaluated in the steady state regime. Gas composition analyses were performed 30 minutes after the process parameters reached their setpoints. Similar stabilization times are reported in the literature [28]. The gas composition analysis system has a high repeatability (< 0.5 % RSD[3]). The effective uncertainty after considerations on the calibration, the sampling system and the development of analytical sequences is $\pm 0.3\ \%v/v$ [46].

[2] Full-Scale
[3] Relative Standard Deviation

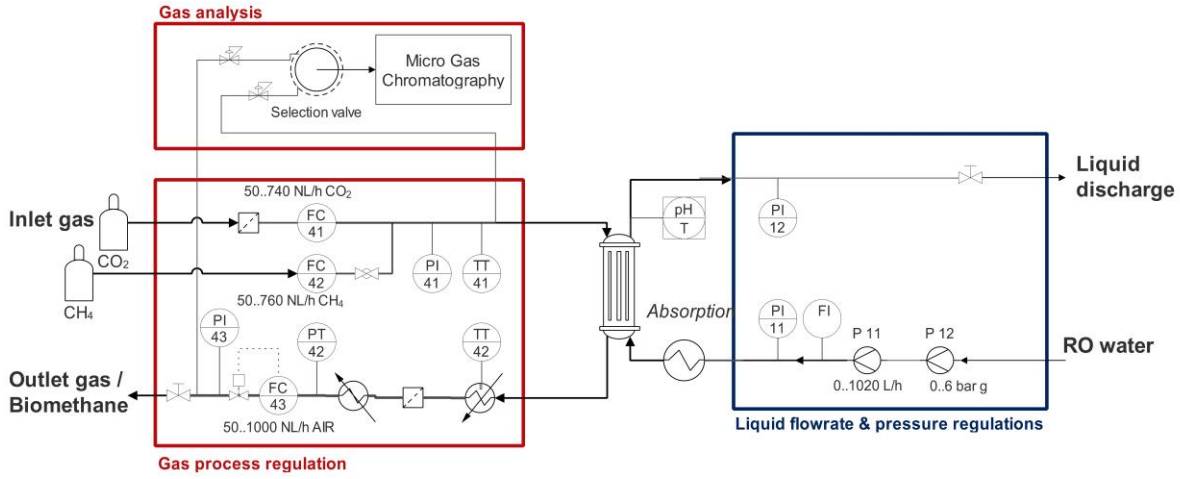

Figure 2 – Experimental set-up for CO_2 absorption from a gas mixture in membrane contactor

A 2.5'' x 8'' Liqui-Cel® Extra-Flow module with hollow fibers of type X-50 was chosen since it is equipped with a central baffle as a mixing element to enhance mass transfer. It is also the smallest item of an available range of industrial contactors. The geometrical features of the module are summarized in Table 2, together with the characteristics of the X-50 hollow fiber. The contact angle between water and the PP membrane material in air was measured to be 121.6° [47]. The breakthrough pressure of the membrane was calculated to be 51 bar g according to the formula [47]:

$$\Delta P_{break} = -\frac{4\,\gamma_{water}\,\cos\theta}{d_{p,mean}} \qquad \text{Eq. 1}$$

Parameter		Value	Source
External fiber area $\boldsymbol{S}$		$1.4\ m^2$	Membrana
Inner radius of the fiber bundle $\boldsymbol{R_i}$		$1.10 \times 10^{-2}\ m$	[48,49]
Outer radius of the fiber bundle $\boldsymbol{R_o}$		$2.32 \times 10^{-2}\ m$	[48]
Thickness of the annular gap between the cartridge and the fiber bundle		$3 \times 10^{-3}\ m$	Membrana
Fiber length $\boldsymbol{L_f}$		$0.203\ m$	[48,49]
Fiber effective length $\boldsymbol{L_f^{eff}}$		$0.146\ m$	[48]
Number of fibers $\boldsymbol{N_f}$		10 200	[49]
Specific area $\boldsymbol{a}$	External fiber area against effective fiber bundle volume	$7\,334\ m^2/m^3$	Calculated
	External fiber area against module external volume	$4\,089\ m^2/m^3$	Calculated
Membrane material		Polypropylene (PP)	Membrana
Inner fiber diameter $\boldsymbol{d_{fi}}$ $[\boldsymbol{\mu m}]$		220	Membrana
External fiber diameter $\boldsymbol{d_{fo}}$ $[\boldsymbol{\mu m}]$		300	Membrana
Porosity[4] $\boldsymbol{\varepsilon_m}$ [%]		40	Membrana
Tortuosity $\boldsymbol{\tau_m}$ $[-]$		3	Membrana
Average pore diameter $\boldsymbol{d_{p,mean}}$ $[\boldsymbol{\mu m}]$		0.03	Membrana
Maximum liquid operating pressure (for $\boldsymbol{T < 40\ °C}$) $[\boldsymbol{bar\ g}]$		7.2	Membrana

Table 2 – Geometric features of the 2.5" x 8" Extra-Flow module equipped with type X-50 hollow fibers

[4] Data from membrane provider

In order to avoid mass transfer issues related to membrane wetting, the membrane module was dried overnight (>6h) with a constant dry air flow ($900\ Nl/h$) at atmospheric pressure and room temperature as previously reported [24,30].

3.2 Experimental operating conditions

The purpose of this work was to explore CO_2 absorption under a wide range of gas composition and flowrates. Three experimental series presented in Table 3 were designed. The gas pressure was set to 5.0 bar g as the absorption is thermodynamically favored under pressure. The transmembrane pressure is chosen at 0.5 bar g, in accordance with the literature, to avoid gas dispersion into the liquid phase [26]. A typical biogas composition is upgraded to biomethane in the first series, with variation in the gas flowrate to obtain different biomethane quality. Then, the effect of the inlet gas composition is investigated in Series 2 and 3. In Series 2, the flowrates are comparable to Series 1 while the gas-to-liquid ratio is set to its maximum in Series 3 (according to the manufacturer guidelines on applicable flowrates) in order to limit the variation in the gas composition across the module, due to the resulting lower CO_2 removal compared to a lower gas-to-liquid ratio. The experiments were performed within a single week to avoid experimental deviation.

Series		**1**	**2**	**3**
Inlet gas flowrate $\mathbf{Q_g^{in}}$	10^{-5} $\mathrm{Nm^3/s}$	4.1 – 23.3	14.6	20.8
Water flowrate $\mathbf{Q_l}$	10^{-5} $\mathrm{m^3/s}$	5.83	5.83	1.67
Gas pressure $\mathbf{P_g}$	bar g	5.0	5.0	5.0
Liquid pressure $\mathbf{P_l}$	bar g	5.5	5.5	5.5
Liquid temperature $\mathbf{T_l}$	K	294	294	294
Inlet gas composition $\mathbf{y_{CO_2}^{in}}$	%v/v	40	10-90	40 - 90

Table 3 – Range of the operating parameters for the three series of experiments

3.3 Data processing

The experiments are assessed under two indicators. The range of the CO_2 gas fraction from the inlet to the outlet, $y_{CO_2}^{out}$, which provides the different gas compositions within the contactor. The absorbed CO_2 flux $J_{CO_2}^{abs}$ is calculated according to Eq. 2:

$$J_{CO_2}^{abs} = \frac{y_{CO_2}^{in} Q_g^{in} - y_{CO_2}^{out} Q_g^{out}}{S} \qquad \text{Eq. 2}$$

In the following, the results are displayed in the figures depending on the inlet CO_2 flowrate Q_{g,CO_2}^{in}.

4 Mass transfer modelling

4.1 Model assumptions

The present work is an adaptation of a previously published model [30], from the case of pure CO_2 physical absorption to the one of a binary mixture. It aims at providing a predictive tool for several CO_2 capture applications. The model describes the internal geometry with the central diverting baffle (Figure 3) and predict local mass transfer coefficients from a resistance-in-series model (see Section 4.2). The process is simulated at steady state. In this paper, only the membrane dry mode is considered since it was previously highlighted that wetting has little impact on the CO_2 absorbed flux in the considered range of liquid flowrate ($< 5 \times 10^{-5}\ m^3/s$) [30].

The solvent hydrodynamics in the shellside is described by the Darcy's law. The fiber bundle is considered as an anisotropic porous medium.

$$\overrightarrow{u_l} = -\frac{\overline{\overline{\kappa_l}}}{\mu_l} \nabla P_l \qquad \text{Eq. 3}$$

where $\overrightarrow{u_l}$ the liquid velocity, P_l the liquid pressure, μ_l the dynamic viscosity and $\overline{\overline{\kappa_l}}$ the permeability tensor of the porous medium.

Table 4 summarizes the assumptions made for the absorption of pure CO_2 only and for the additional ones made for the case of a binary gas mixture.

Absorption of pure CO_2 [30]	Absorption of a binary mixture
1. Isothermal operation; 2. Gas flowing in the lumenside under constant gas pressure (no pressure drop); 3. Ideal gas behavior; 4. Henry's law is valid; 5. Membrane features (average pore size, pore size distribution, porosity, thickness, hydrophobicity and tortuosity) are uniform in the module; 6. Membrane properties are constant over time; 7. Solvent evaporation is neglected (low vapor pressure); 8. No phase entrainment across the membrane.	1. The gas phase is a binary gas mixture 2. Both components are absorbed 3. Resistance in the gas phase is neglected against resistance in the liquid phase 4. No interaction between mixture components regarding thermodynamic equilibriums.

Table 4 – Assumptions of the mass transfer model

4.2 Mass transfer coefficients

In our module configuration, the overall mass transfer resistance relative to the liquid phase K_L is expressed by [30]:

$$\frac{1}{K_L d_{fo}} = \frac{1}{k_l d_{fo}} + \frac{H^{cc}}{k_m\, d_{ln}} + \frac{H^{cc}}{k_g\, d_{fi}} \qquad \text{Eq. 4}$$

where H^{cc} is the dimensionless Henry coefficient, k_φ is the mass transfer coefficient for the phase φ and d_{fo}, d_{fi}, d_{ln} are respectively the outer, inner and logarithmic mean diameters of the fibers.

In a first approach, the resistance in the gas phase and gas concentration radial variation in a lumen are neglected against the resistance in the liquid phase. Indeed, under a moderate gas pressure ($P_g = 5\ bar\ g$), the diffusion coefficient in the gas phase is 3 orders of magnitude higher that the one in the liquid phase ($D^g_{CO_2} \sim 10^{-6}\ m^2.s^{-1}$ against $D^l_{CO_2-water} \sim 10^{-9}\ m^2.s^{-1}$). Moreover, the dimensionless Henry coefficients are below 1 (9.2×10^{-1} and 3.4×10^{-2} for CO_2 and CH_4 respectively [50]).

The liquid mass transfer resistances are derived from the calculation of the Sh_l number according to the Chilton-Colburn correlation optimized in our previous paper:

$$Sh_l = 3.45\ Re_l^{0.42} Sc_l^{\frac{1}{3}} \qquad \text{Eq. 5}$$

In this equation, the dimensionless numbers are defined based on local conditions. Indeed, the description of the shellside hydrodynamics in a porous medium displays a non-uniform Reynolds number. The dimensionless numbers and subsequent mass transfer coefficients are then estimated locally:

$$Re_l = \frac{d_{fo}\|\vec{u}_l\|}{\nu_l} \qquad \text{Eq. 6}$$

$$Sh_l = \frac{d_{fo} k_l}{D_l} \qquad \text{Eq. 7}$$

$$Sc_l = \frac{\nu_l}{D_l} \qquad \text{Eq. 8}$$

The membrane mass transfer coefficient k_m, calculated under the membrane dry mode, is a combination of molecular and Knudsen diffusions according to Bosanquet's law (details in Appendix) [34]:

$$k_m = k_{m,dry} = \frac{D_{g,eff}\varepsilon_m}{\tau_m \delta_m} \quad \text{Eq. 9}$$

$$\frac{1}{D_{g,eff}} = \frac{1}{D_{mol}} + \frac{1}{D_{Kn}} \quad \text{Eq. 10}$$

4.3 Model equations

4.3.1 Shell side

The same set of equations is governing the CO_2 and the CH_4 mass transfer. The CH_4 mass balance equation is written:

$$\nabla.\left(\overrightarrow{u_l}.C^l_{CH_4}\right) = \frac{\varepsilon_{bed,l}}{\tau_{bed,l}} D^l_{CH_4} \Delta C^l_{CH_4} + r_{CH_4} \quad \text{Eq. 11}$$

where $C^l_{CH_4}$ is the dissolved CH_4 concentration in the liquid and $D^l_{CH_4}$ its diffusivity in the liquid. $\varepsilon_{bed,l}$ is the shell side porosity. It was calculated as the contactor volume minus the fibers volume using the manufacturer data (Table 2). $\tau_{bed,l}$ is the shell side tortusotiy, it is not known. A value of was taken as a rough estimate and is thought to be valid given the contactor aspect ratio.

The source term r_{CH_4} is the CH_4 flowrate transferred from the gas phase to the liquid phase in $mol.m^{-3}.s^{-1}$:

$$r_{CH_4} = \varepsilon_m K_{L,CH_4} a\left(H^{cc}_{CH_4} C^g_{tot} y_{CH_4} - C^l_{CH_4}\right) \quad \text{Eq. 12}$$

where K_{L,CH_4} is the local mass transfer coefficient of methane ($m.s^{-1}$), a the specific area ($m^2.m^{-3}$), $H^{cc}_{CH_4}$ the dimensionless Henry coefficient, $C^{\varphi}_{CH_4}$ the concentration of CH_4 in the bulk of phase φ.

4.3.2 Lumen side

Since the fiber lumenside is not interconnected, the gas is numerically forced to flow only in the direction of the fibers. Hence a 1D model can be used to describe the gas phase behavior. Similarly to the liquid phase, the gas flow in the lumenside is described by the Darcy's law:

$$\overrightarrow{u_g} = -\frac{\kappa_g}{\mu_g}\frac{dP_g}{dz} \quad \text{Eq. 13}$$

where $\overrightarrow{u_g}$ is the gas velocity, P_g the gas pressure, μ_g its dynamic viscosity and κ_g the permeability tensor of the porous medium. The permeability $\overline{\overline{\kappa_g}}$ is derived from the Poiseuille equation for a viscous flow in a cylindrical tube: (Eq. 14).

$$\kappa_g = \varepsilon_{bed,g}\frac{d^2_{fi}}{32} \quad \text{Eq. 14}$$

The gas flow is controlled by the mass continuity equation in which the gas-liquid mass transfer terms r_i appear:

$$\frac{d}{dz}\left(\rho_g \overrightarrow{u_g}\right) = -\kappa_g \nabla.\left(\frac{C^g_{tot} M_g}{\mu_g}\frac{dP_g}{dz}\right) = -\sum_i r_i M_i \quad \text{Eq. 15}$$

where ρ_g is the gas density, C^g_{tot} the total gas molar concentration, r_i the source term for species i, M_g and M_i the respective molar masses of the gas phase mixture and species i.

The mass balance equation on the gas phase for component i controls the evolution of its molar fraction y_i:

$$\frac{d}{dz}\left(\overrightarrow{u_g}.C^g_{tot} y_i\right) = \frac{\varepsilon_{bed,g}}{\tau_{bed,g}} D^g_i C^g_{tot}\frac{d^2 y_i}{dz^2} - r_i \quad \text{Eq. 16}$$

where $\varepsilon_{bed,g}$ (calculated with manufacturer data) and $\tau_{bed,g}$ (taken equal to 1) are the porosity and tortuosity of the fiber bed regarding the gas phase, y_i is the gas molar fraction, D^g_i the diffusion coefficient in the gas mixture and r_i the source term of species i. C^g_{tot} is considered constant along the membrane module as no pressure drop has been observed during the experiments ($\Delta P < 0.05\ bar$).

4.4 Geometry and boundary conditions

The axial geometry of the membrane module allows the reduction to a two dimensions problem. Two different meshes are superimposed to respectively describe the gas and the liquid phases (Figure 3). The model simulates the outlet compositions and flowrates from input parameters (inlet composition and flowrates, operating pressures and temperatures).

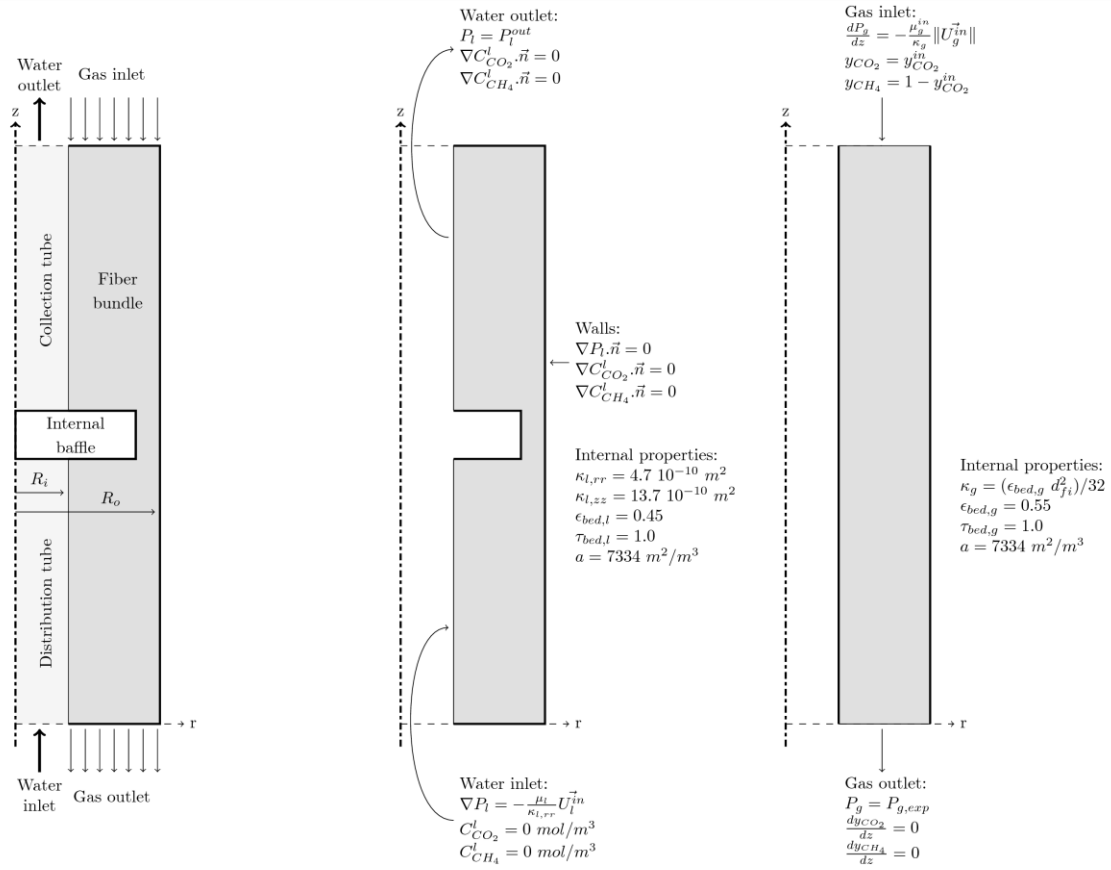

Figure 3 – Module geometry with model inlet and boundary conditions (a) Internal module geometry (b) Liquid flow on the shellside (c) Gas flow on the lumenside

The model was implemented under the open source CFD framework OpenFOAM. The same mesh was used for both the liquid and the gas phases: the convergence was achieved using a 9000 square cells mesh. Mass imbalance was verified to be below 10^{-4}. The solver tolerance was set to 10^{-9} for all the numerical fields. The runtime for a single simulation is about 20 minutes on a single thread (Intel Core i7-4910 MQ Haswell at 2.90 GHz, 16 G DDR3 1600 MHz).

5 Comparison of experimental and numerical results

The experimental results are presented in Table 5. In the first series, the biogas mixture (40% CO_2, 60% CH_4) is further upgraded from $y_{CO_2}^{out} = 28.1\%$ down to 1.9% as the gas flowrate Q_g^{in} decreases. The gas composition is then highly variable. In the Series 2 with a varying inlet gas composition, the CO_2 gas fraction decreases by a maximum of 12.3 points between the inlet and outlet. In the Series 3, this variation is minimized with a high gas-to-liquid ratio: the gas partial pressures are almost constant across the mass exchanger. The results on the absorbed CO_2 fluxes are discussed in the following paragraphs. In the meantime, the corresponding simulations were run to validate the model. The relative numerical error on the CO_2 absorbed flux is calculated according to:

$$\varepsilon_{rel,J_{CO_2}} = \frac{J^{abs}_{CO_2,num} - J^{abs}_{CO_2,exp}}{J^{abs}_{CO_2,exp}} \qquad \text{Eq. 17}$$

Series	Q_g^{in} $(10^{-5}$ $Nm^3/$ $s)$	Q_l $(10^{-5}$ $m^3/s)$	$y_{CO_2}^{in}$	$y_{CO_2}^{out}$	CO_2 removal rate	$J_{CO_2}^{abs}$ $[10^{-4}\ mol_{CO_2}.m^{-2}.s^{-1}]$
1	4.1	5.83	40	1.9	101%	5.24
	5.8			5.4	95%	7.07
	9.9			15.2	78%	9.84
	14.6			22.5	61%	11.4
	18.7			26.1	51%	12.2
	23.3			28.1	45%	13.5
2	14.6	5.83	10	6.3	40%	1.88
			40	27.7	46%	8.53
			70	59.6	46%	15.0
			90	80.2	68%	28.3
3	20.8	1.67	40	34.5	21%	5.57
			70	65.7	26%	12.0
			90	87.6	29%	17.1

Table 5 – Experimental results for the absorption of CO_2 in a CO_2/CH_4 mixture

5.1 Influence of the flowrate ratio

The absorbed CO_2 fluxes both from experimental data and numerical simulations are compared in Figure 4 for the Series 1. The continuous line is the equivalent inlet CO_2 flux, which is then the maximum absorbed CO_2 flux. The experimental absorbed CO_2 flux is increasing with the inlet gas flowrate according to a square root function while the numerical flux follows a linear trend. As the inlet gas flow increases, the CO_2 concentration will be higher, thus increasing the mass transfer potential. The two first points of this series are not discriminant regarding mass transfer efficiency since nearly all the inlet CO_2 flow is removed (99 and 95 % respectively). A variation in the mass transfer coefficient will not be observed for these experiments. However, as the inlet CO_2 flowrate is increasing proportionally to the total gas flowrate, the relative numerical error is increasing from -8 % at $Q_g^{in} = 4.1 \times 10^{-5} Nm^3/s$ to 75 % at $Q_g^{in} = 23.3 \times 10^{-5} Nm^3/s$.

Since the numerical model had been previously validated for the absorption of pure CO_2, the observed deviation between the numerical and experimental results may be explained by a lower mass transfer efficiency in the presence of methane.

5.2 Influence of the inlet gas composition

The absorbed CO_2 flux is increasing with the CO_2 fraction at the gas inlet, for both Series 2 and 3 (Figure 5). With a higher CO_2 concentration, the mass transfer potential increases leading to a rise in the absorbed CO_2 flux. In Series 2, is multiplied by a factor 15 between the two extreme concentrations (and for and respectively). Yet this increase by a factor 15, while applying a factor 9 to the inlet parameters, underlines the existence of a non-trivial behavior.

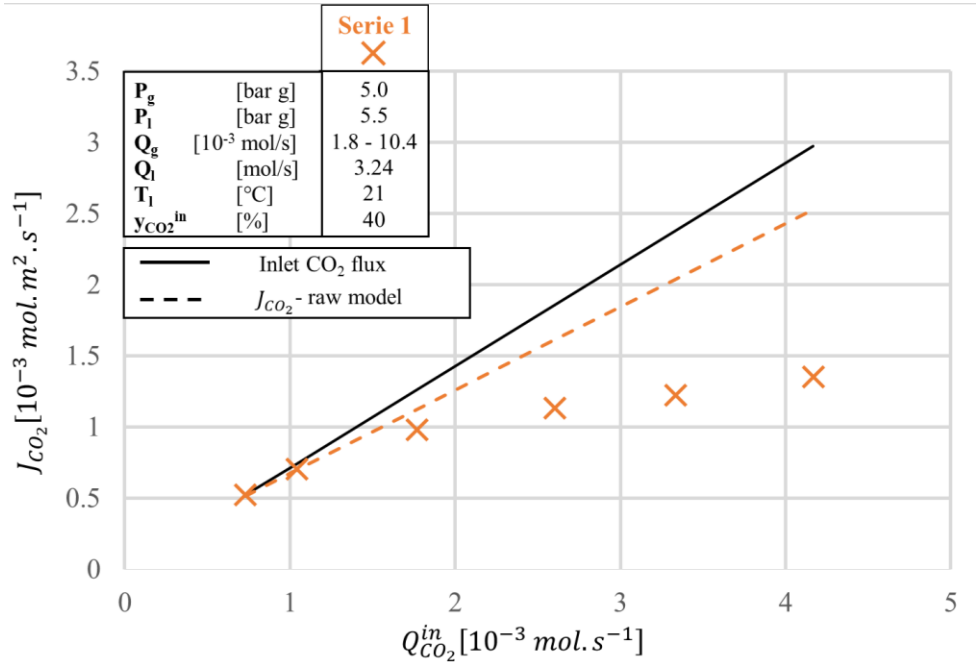

Figure 4 – Influence of the inlet gas flowrate on the absorbed CO_2 flux

The deviation between the experimental and numerical absorbed CO_2 fluxes is confirmed for both Series 2 and 3. In Series 2, the relative error on the absorbed flux is increasing as the inlet CO_2 fraction is reduced: the deviation of 20 % at $y_{CO_2}^{in} = 90$ % rise up to 135 % at $y_{CO_2}^{in} = 10$ %. This trend is confirmed with Series 3 where the relative error on $J_{CO_2}^{abs}$ is rising with a decreasing inlet concentration (from 33% to 79 % for an inlet CO_2 fraction of 40 and 90 % respectively). In this series, the gas-to-liquid ratio was maximized to observe a small variation in the partial gas pressures (Table 5). The high relative error observed implies that the model mass transfer description is incomplete.

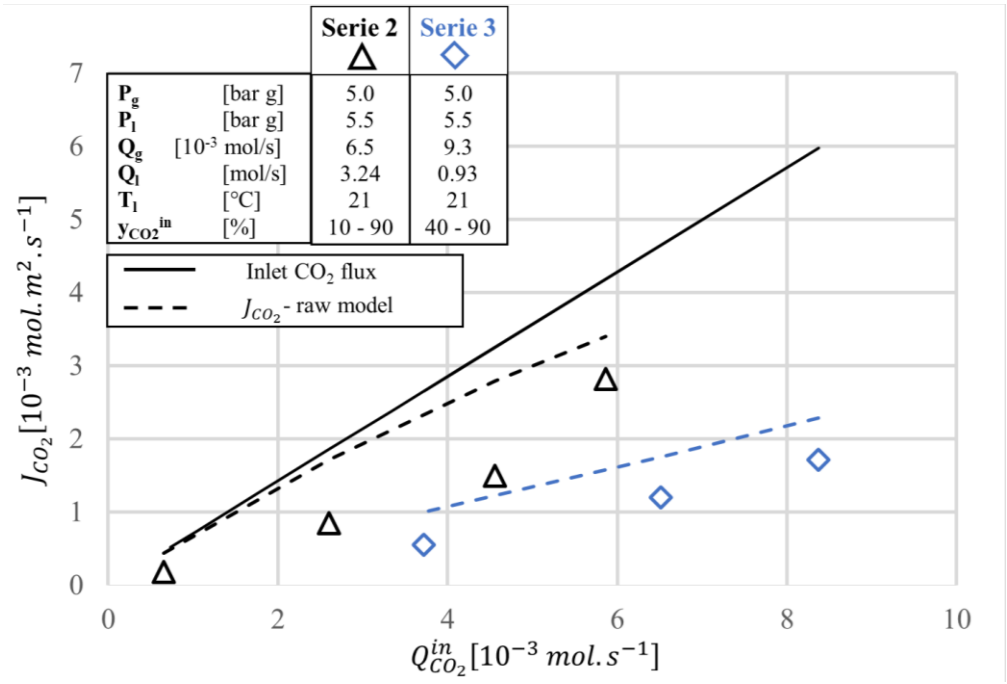

Figure 5 – Influence of the inlet gas composition on the absorbed CO_2 flux

6 Discussion

The numerical model had previously been validated for the absorption of pure CO_2 into water. However, the comparison in the previous section with experimental data for the case of a CO_2/CH_4 binary mixture led to a high deviation in the absorbed CO_2 flux. Moreover, this deviation was found to increase with a diminishing CO_2 gas fraction. Therefore, there is an additional mass transfer resistance which has not been modelled. Based on these finding; this resistance would both have a constant component and dependent on gas composition. Assuming that the presence of the methane in the gas mixture is not affecting the liquid shellside hydrodynamics, this resistance has to be located in the membrane itself.

6.1 Knudsen diffusion

In the membrane, both molecular and Knudsen diffusions are at stake in the membrane pores, with a Knudsen number around 0.34. The respective diffusivities are calculated in the conditions of the experiments ($P_g = 5\ bar\ g, T = 21°C$). The binary molecular diffusivity is $D_{CO_2-CH_4} = 2.93 \times 10^{-6}\ m^2.s^{-1}$ while the Knudsen diffusivity is respectively $3.76 \times 10^{-6}\ m^2.s^{-1}$ and $6.24 \times 10^{-6}\ m^2.s^{-1}$ for CO_2 and CH_4 respectively. The effective diffusivity of a component A is then calculated from Eq. 18.

$$\frac{1}{D_A^{eff}} = \frac{1}{D_{AB}} + \frac{1}{D_{A,Kn}} \qquad \text{Eq. 18}$$

Even though this approach was successfully used by authors, they were working in conditions where the liquid resistance was the limiting one and with membrane exhibiting much larger pores [34,51–53]. Hence this description is in the general case be far too simplistic. Indeed, when the value of the Knudsen number indicates the transfer mode is in the transition zone, the whole classical diffusion equations have to be adapted and solved. In our case, the basic mass transfer equation:

$$\overrightarrow{N_A} = y_A\left(\overrightarrow{N_A} + \overrightarrow{N_B}\right) + \overrightarrow{J_A} \qquad \text{Eq. 19}$$

Becomes a much more complex one, taking both Knudsen and molecular contributions into account:

$$\overrightarrow{N_A} = y_A \frac{D_{A,Kn}}{D_{A,Kn} + \frac{\varepsilon_m}{\tau_m} D_{AB}}\left(\overrightarrow{N_A} + \overrightarrow{N_B}\right) - \left(\frac{1}{\frac{\varepsilon_m}{\tau_m} D_{AB}} + \frac{1}{D_{A,Kn}}\right)^{-1} C_{tot}^g \nabla y_A \qquad \text{Eq. 20}$$

Luckily, and with the introduction a variable called the separation factor α, one can integrate this equation in the membrane phase [54], yielding:

$$\alpha = -\sqrt{\frac{M_{CO2}}{M_{CH4}}} \qquad \text{Eq. 21}$$

$$N_A^m = \frac{\frac{\varepsilon_m}{\tau_m} D_{AB} C_{tot}^g}{(1+\alpha) d_{ln}} \ln\left(\frac{1 - y_{A,m}^{out}(1+\alpha) + \frac{\varepsilon_m}{\tau_m} D_{AB} \Big/ D_{Kn,A}}{1 - y_{A,m}^{in}(1+\alpha) + \frac{\varepsilon_m}{\tau_m} D_{AB} \Big/ D_{Kn,A}}\right) \qquad \text{Eq. 22}$$

As expected from experimental observations, this expression contains both a constant term (associated to Knudsen flow) and term varying with gas composition. Finally, in order to validate this approach, this expression was substituted to the former membrane term in the model before running once again.

6.2 Advanced model results

Figure 6 reports the comparison between the new model predictions and the experimental data. Both the trends and the absolute values (average $\varepsilon_{rel,J_{CO_2}} = 6.3\%$) of the three series are well captured by the new model. Despite the good description of the absorbed flux J_{CO_2}, significant errors can be observed with different operating conditions (average $\varepsilon_{rel,J_{CO_2}}$ min/max -34/+48%). They can be explained by three reasons:

- the mass balance precision is limited by the analytical sensors (gas flowmeters and gas composition analysis). This limitation is explained by the wide range of experimental conditions covered ($Q_g = 147 - 750\ NL.h^{-1}$, $y_{CO_2}^{in} = 10 - 90\ \%$) which induces an increased uncertainty on the sensors;

- the operating conditions studied in these 3 series fully cover the possibilities of the pilot equipment. Modelling mass transfer is rendered more difficult by such a wide experimental range and the hypothetical change in the mass transfer limiting phenomenon nature;
- no fitting parameter was introduced in the model. Hence, only manufacturer geometrical data were used. As a matter of fact, those parameters are not known with a high confidence, e.g. only one significant digit, … Increasing the measurement accuracy of those membrane characteristics would improve the model performances.

Considering uncertainty issues and the wide range of operating conditions, the numerical performances obtained with the advanced model are deemed very satisfactory. This is all the more true when one keeps in mind that no fitting factor has been included. Indeed, only membrane geometrical characteristic have been used in this work.

As take home point, this experimental and numerical investigations have highlighted the effect of the gas composition and flow rate on the mass transfer mechanisms: the presence of a methane is not only decreasing the CO_2 partial pressure in the gas phase but is also significantly affecting the mass transfer efficiency.

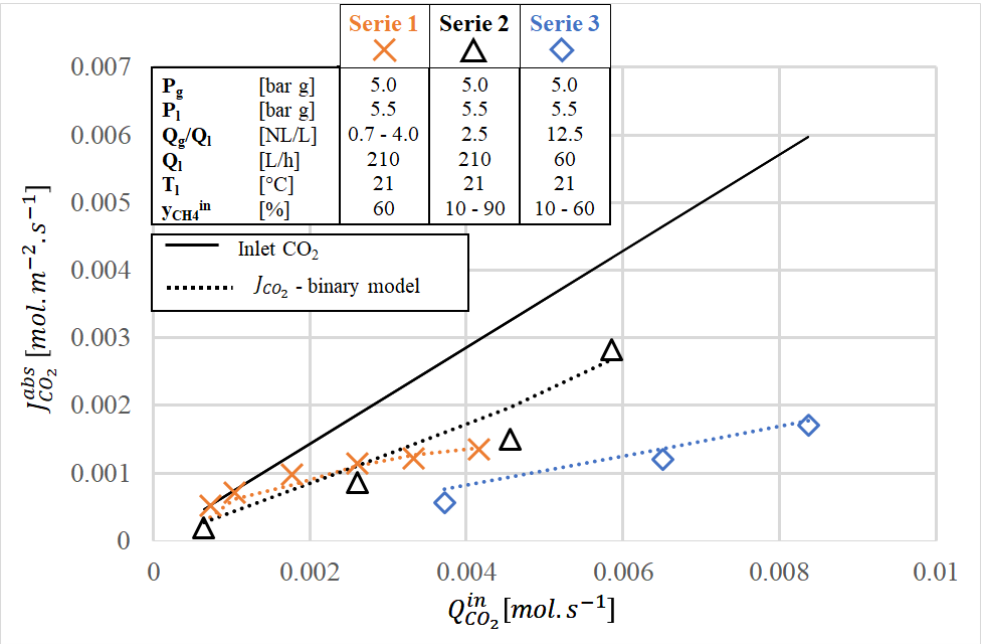

Figure 6 – Advanced model against experimental data: absorbed CO_2 flux

7 Conclusion

The effect of the gas composition and flow rate on the CO_2 physical absorption in a HFMM was experimentally investigated in a CO_2/CH_4 mixture in the membrane dry mode. In accordance with the literature, the absorbed CO_2 flux is found to increase with an increasing CO_2 molar fraction: a factor 15 was found between a 10% and 90% CO_2 molar fraction at the inlet. This rise in the CO_2 partial pressure enhances its solubility, and thus the absorption driving force.

In the meantime, a numerical model describing the absorption of CO_2 in a binary gas mixture, based on the internal module geometry and on a local description of the hydrodynamics was proposed. Mass transfer described by a resistance-in-series model was shown not be adapted to properly represent the physics at stake in a HFMM. Indeed, in order to capture the key phenomena, a proper description of mass transfer in transition zone (Knudsen number around 0.34) is mandatory. Implementing this description allowed the model to accurately describe mass transfer over a wide range of gas composition and flow rate, without relying on any fitted parameter.

This original numerical model can be of interest to broaden scientific understanding of HFMM mass transfer capabilities. Furthermore, as a multi-scale model, only fed with geometrical parameters, it lays the basis for a future scale-up methodology for HFMM.

8 Appendix

8.1 Gas diffusion in the membrane

In a porous media, both molecular and Knudsen diffusions can be at stake. The molecular diffusion also called continuum diffusion refers to the relative motion of different gas species. Knudsen diffusion describes the interactions between the gas molecules and the porous structure: the gas molecule may collide the medium walls more often than other gas molecules. The prevalent diffusion mechanism (molecular and/or Knudsen diffusions) is determined using the Knudsen number Kn (Eq. 23). It compares the molecules mean free path λ calculated according to the kinetic theory of gases [55] to a characteristic length of the medium microstructure (such as the pore mean diameter $d_{p,mean}$). The mean free path λ represents the average distance one gas molecule can travel before colliding another molecule (Eq. 24).

$$Kn = \frac{\lambda}{d_{p,mean}} \qquad \text{Eq. 23}$$

$$\lambda = \frac{k_B T}{\sqrt{2}\pi\eta^2 P_g} \qquad \text{Eq. 24}$$

with k_B the Boltzmann constant $[1.3806 \times 10^{-23}\ m^2.kg.s^{-2}.K^{-1}]$, T the temperature $[K]$, η the particle hard-shell diameter $[m]$ and P_g the gas pressure $[Pa]$.

An example of Knudsen number calculation is provided for CH_4 and CO_2 diffusion through the X-50 fiber in Table 6. The particle hard-shell diameters $\eta_{CH_4} = 380 \times 10^{-12}\ m$ and $\eta_{CO_2} = 390 \times 10^{-12}\ m$ are taken from Hirschfelde [56].

Gas	$\boldsymbol{\lambda}\ [\boldsymbol{nm}]$	$\boldsymbol{Kn}$
$\boldsymbol{CH_4}$	10.5	0.35
$\boldsymbol{CO_2}$	9.99	0.33

Table 6 – Mean free path and Knudsen number into the porous X-50 fiber (T=294 K, P_g = 5 bar g)

Under the process conditions, both molecular and Knudsen diffusions are at stake and must be simultaneously considered using Eq. 10.

The effective diffusivity calculated in the above equation is applicable to straight and perfectly cylindrical pores. To account for the porous medium interconnections and the size distribution of the pores, one must take into account the porosity ε to tortuosity τ ratio.

$$D_A^{eff,porous} = \frac{\varepsilon}{\tau} D_A^{eff} \qquad \text{Eq. 25}$$

8.2 Physico-chemical properties

The developed model requires to estimate physico-chemical properties with a temperature dependence (Table 7).

Property	Unit	Mathematical expression (SI)	Source
$\boldsymbol{D_{CO_2-water}}$	$m^2.s^{-1}$	$5.4711 \times 10^{-15}\ T\ \mu_{water}(T)^{-1.00937}$	[57]
$\boldsymbol{D_{CH_4-water}}$	$m^2.s^{-1}$	$1.1227 \times 10^{-14}\ T\ \mu_{water}(T)^{-0.89297}$	[57]
$\boldsymbol{\nu_{water}}$	$m^2.s^{-1}$	$10^{-6}\exp\left(-3.28285 + \frac{4.56029 \times 10^2}{T - 1.54576 \times 10^2}\right)$	[58]
$\boldsymbol{D^g_{CO_2-CH_4}}$	$m^2.s^{-1}$	$\frac{10^{-7}T^{1.75}}{P\left[(\sum \nu)_A^{1/3} + (\sum \nu)_B^{1/3}\right]^2}\left[\frac{1}{M_A} + \frac{1}{M_B}\right]^{\frac{1}{2}}$	[59]
$\boldsymbol{H^{cc}_{CO_2}}$	–	$3.3564 \times 10^{-4} \times RT \times \exp\left(2400\left(\frac{1}{T} - \frac{1}{298.15}\right)\right)$	[50]
$\boldsymbol{H^{cc}_{CH_4}}$	–	$1.2833 \times 10^{-5} \times RT \times \exp\left(1800\left(\frac{1}{T} - \frac{1}{298.15}\right)\right)$	[50]
$\boldsymbol{D_{Kn,A}}$	$m^2.s^{-1}$	$\frac{4}{3}\ d_{pore}\ \frac{\varepsilon}{\tau}\sqrt{\frac{RT}{2\pi M_A}}$	[60]
$\boldsymbol{\gamma_{water}}$	$N.m^{-1}$	$15\ °C: 73.5 \times 10^{-3}$	[61]

		$20\ °C: 73.0 \times 10^{-3}$	

Table 7 – Physico-chemical properties

The empirical Fuller equation is used to estimate binary diffusion coefficients D_{AB}^{g} [59]. The interactions between the molecules are described by the estimation of an equivalent volume of diffusion $\sum v$ based on the elements of the gas molecule. The relative error between the results derived from the Fuller equation and the Chapman-Eskog theory is below 4 % for binary systems [7]. The molecular volumes are taken from Reid [62]. In the case of unavailable data, the molecular volume is estimated by addition of the atomic volumes.

9 Acknowledgements

This work was supported by the Marne departmental council, the Champagne-Ardenne regional council and Reims Metropole through the Biotechnology Chair of CentraleSupelec.

10 Nomenclature

Latin symbols

a	Specific exchange area
C_i^{φ}	Volumic molar concentration of component i in phase φ
d	Diameter
D_A^{φ}	Diffusivity of solute A in the phase φ
D_{AB}	Gaseous diffusivity of specie A in specie B
H^{cc}	Henry coefficient relative to liquid and gas molar concentrations
J_{i}^{abs}	Absorbed flux of component i through the membrane
Kn	Knudsen number
$K_{\varphi,i}^{0}$	Overall mass transfer coefficient of specie i relative to the phase φ in $mol.m^{-2}.s^{-1}$
$K_{\varphi,i}$	Overall mass transfer coefficient of specie i relative to the phase φ in $m.s^{-1}$ ($i = CO_2$ if not specified)
$k_{\varphi,i}$	Mass transfer coefficient of specie i relative to the resistance of the phase φ in $m.s^{-1}$
L_f	Length of the fiber
M_i	Molar mass of specie i
$\vec{n}$	Normal vector
N_A	Molar flux of specie A

N_f	Number of fibers
P_i	Gas partial pressure of component i
P_{φ}	Total pressure of phase φ
ΔP	Transmembrane pressure
Q_g	Gas volumetric flowrate
Q_l	Liquid flowrate
r	Radius
r_i	Source term of specie i
R	Ideal gas constant
R_i/R_o	Inner/Outer radius of the fiber bundle
R_{CH_4}	Methane recovery ratio
R_{φ}	Mass transfer resistance of the phase φ
Re	Reynolds number
S	Exchange area
Sc	Schmidt number
Sh	Sherwood number
T_{φ}	Temperature of phase φ
$\overrightarrow{u_{\varphi}}$	Velocity of the phase φ
x_i	Molar fraction of component i in the liquid phase
y_i	Molar fraction of component i in the gas phase

Greek symbols

α	Separation factor
γ	Surface tension
δ	Thickness
ε	Porosity
$\varepsilon_{bed,\varphi}$	Porosity of the porous medium related to phase φ
ε_{rel}	Relative error
η	Membrane wetting fraction
$\overline{\overline{\kappa_{\varphi}}}$	Permeability tensor of the porous medium related to phase φ

λ	Molecule mean free path
Φ	Packing fraction in the bundle of fibers (%)
μ_{φ}	Dynamic viscosity of phase φ
ν	Kinematic viscosity
ρ	Volumetric mass density
τ	Tortuosity

Superscripts

abs	Relative to the absorbed flow
$bulk$	Relative to the bulk
eff	Effective
in	Relative to the inlet flow of the HFMM

out	Relative to the outlet flow of the HFMM

Subscripts

bed	Relative to the porous medium
$break$	Breakthrough pressure
CH_4	Methane
CO_2	Carbon dioxide
exp	Relative to the experiment
fi	Relative to the hollow fiber inner side
$fiber$	Relative to the hollow fiber

fo	Relative to the hollow fiber outer side
m	Relative to the membrane
num	Relative to the numerical model
ML	Logarithmic mean
p	Relative to the pore
tot	Total

11 References

[1] M.H. Al-Marzouqi, S.A.M. Marzouk, N. Abdullatif, High pressure removal of acid gases using hollow fiber membrane contactors: Further characterization and long-term operational stability, J. Nat. Gas Sci. Eng. 37 (2017) 192–198. doi:10.1016/j.jngse.2016.11.039.

[2] S. Zhao, P.H.M. Feron, L. Deng, E. Favre, E. Chabanon, S. Yan, J. Hou, V. Chen, H. Qi, Status and progress of membrane contactors in post-combustion carbon capture: A state-of-the-art review of new developments, J. Membr. Sci. 511 (2016) 180–206. doi:10.1016/j.memsci.2016.03.051.

[3] P.H.M. Feron, Absorption-Based Post-Combustion Capture of Carbon Dioxide, Woodhead Publishing, 2016.

[4] A. McLeod, B. Jefferson, E.J. McAdam, Quantifying the loss of methane through secondary gas mass transport (or “slip”) from a micro-porous membrane contactor applied to biogas upgrading, Water Res. 47 (2013) 3688–3695. doi:10.1016/j.watres.2013.04.032.

[5] S. Vogler, A. Braasch, G. Buse, S. Hempel, J. Schneider, M. Ulbricht, Biogas Conditioning Using Hollow Fiber Membrane Contactors, Chemie Ingenieur Technik. 58 (2013) 1254–1258. doi:10.1002/cite.201200235.

[6] A.C. Sun, W. Kosar, Y. Zhang, X. Feng, Vacuum membrane distillation for desalination of water using hollow fiber membranes, J. Membr. Sci. 455 (2014) 131–142. doi:10.1016/j.memsci.2013.12.055.

[7] M. Roustan, Transferts gaz-liquide dans les procédés de traitement des aux et des effluents gazeux, Tec & Doc, 2003.

[8] J. Elhajj, M. Al-Hindi, F. Azizi, A Review of the Absorption and Desorption Processes of Carbon Dioxide in Water Systems, Ind. Eng. Chem. Res. 53 (2014) 2–22. doi:10.1021/ie403245p.

[9] E.L. Paul, V.A. Atiemo-Obeng, S.M. Kresta, eds., Handbook of industrial mixing: science and practice, Wiley-Interscience, Hoboken, N.J, 2004.

[10] P. Luis, B. Van der Bruggen, T. Van Gerven, Non-dispersive absorption for CO2 capture: from the laboratory to industry, J. Chem. Technol. Biotechnol. 86 (2011) 769–775. doi:10.1002/jctb.2614.

[11] J. Kerber, J.-U. Repke, Mass transfer and selectivity analysis of a dense membrane contactor for upgrading biogas, J. Membr. Sci. 520 (2016) 450–464. doi:10.1016/j.memsci.2016.08.008.

[12] D. Albarracin Zaidiza, Modelling of Hollow Fibre Membrane Contactors : Application Post-combustion Carbon Dioxide Capture, Université de Lorraine, LRGP, 2016. http://www.theses.fr/2016LORR0035.

[13] S. Masoumi, M.R. Rahimpour, M. Mehdipour, Removal of carbon dioxide by aqueous amino acid salts using hollow fiber membrane contactors, J. CO2 Util. 16 (2016) 42–49. doi:10.1016/j.jcou.2016.05.008.

[14] G. Hu, N.J. Nicholas, K.H. Smith, K.A. Mumford, S.E. Kentish, G.W. Stevens, Carbon dioxide absorption into promoted potassium carbonate solutions: A review, Int. J. Greenh. Gas Control. 53 (2016) 28–40. doi:10.1016/j.ijggc.2016.07.020.

[15] D. deMontigny, P. Tontiwachwuthikul, A. Chakma, Comparing the Absorption Performance of Packed Columns and Membrane Contactors, Ind. Eng. Chem. Res. 44 (2005) 5726–5732. doi:10.1021/ie040264k.

[16] W. Rongwong, C. Fan, Z. Liang, Z. Rui, R.O. Idem, P. Tontiwachwuthikul, Investigation of the effects of operating parameters on the local mass transfer coefficient and membrane wetting in a membrane gas absorption process, J. Membr. Sci. 490 (2015) 236–246. doi:10.1016/j.memsci.2015.04.071.

[17] H. Gao, S. Liu, G. Gao, X. Luo, Z. Liang, Hybrid behavior and mass transfer performance for absorption of CO2 into aqueous DEEA/PZ solutions in a hollow fiber membrane contactor, Sep. Purif. Technol. 201 (2018) 291–300. doi:10.1016/j.seppur.2018.03.027.

[18] K. Kim, D.Y. Kim, K.R. Lee, J.-I. Han, Electricity generation from iron EDTA-based liquid redox sulfur recovery process with enhanced stability of EDTA, Energy Convers. Manag. 76 (2013) 342–346. doi:10.1016/j.enconman.2013.07.063.
[19] Z. Zhang, Y. Yan, L. Zhang, Y. Chen, J. Ran, G. Pu, C. Qin, Theoretical Study on CO2 Absorption from Biogas by Membrane Contactors: Effect of Operating Parameters, Ind. Eng. Chem. Res. 53 (2014) 14075–14083. doi:10.1021/ie502830k.
[20] M.H. Al-Marzouqi, M.H. El-Naas, S.A.M. Marzouk, M.A. Al-Zarooni, N. Abdullatif, R. Faiz, Modeling of absorption of CO2 in membrane contactors, Sep. Purif. Technol. 59 (2008) 286–293. doi:10.1016/j.seppur.2007.06.020.
[21] S. Atchariyawut, R. Jiraratananon, R. Wang, Separation of CO2 from CH4 by using gas–liquid membrane contacting process, J. Membr. Sci. 304 (2007) 163–172. doi:10.1016/j.memsci.2007.07.030.
[22] Z. Zhang, Comparisons of various absorbent effects on carbon dioxide capture in membrane gas absorption (MGA) process, 2016.
[23] Z. Zhang, F. Chen, M. Rezakazemi, W. Zhang, C. Lu, H. Chang, X. Quan, Modeling of a CO2-Piperazine-Membrane Absorption System, 2017.
[24] M. Mavroudi, S.P. Kaldis, G.P. Sakellaropoulos, A study of mass transfer resistance in membrane gas–liquid contacting processes, J. Membr. Sci. 272 (2006) 103–115. doi:10.1016/j.memsci.2005.07.025.
[25] S.-J. Kim, A. Park, S.-E. Nam, Y.-I. Park, P.S. Lee, Practical designs of membrane contactors and their performances in CO2/CH4 separation, Chem. Eng. Sci. 155 (2016) 239–247. doi:10.1016/j.ces.2016.08.018.
[26] A. Park, Y.M. Kim, J.F. Kim, P.S. Lee, Y.H. Cho, H.S. Park, S.E. Nam, Y.I. Park, Biogas upgrading using membrane contactor process: Pressure-cascaded stripping configuration, Sep. Purif. Technol. 183 (2017) 358–365. doi:10.1016/j.seppur.2017.03.006.
[27] F. Porcheron, S. Drozdz, Hollow fiber membrane contactor transient experiments for the characterization of gas/liquid thermodynamics and mass transfer properties, Chem. Eng. Sci. 64 (2009) 265–275. doi:10.1016/j.ces.2008.09.035.
[28] H.-Y. Zhang, R. Wang, D.T. Liang, J.H. Tay, Modeling and experimental study of CO2 absorption in a hollow fiber membrane contactor, J. Membr. Sci. 279 (2006) 301–310. doi:10.1016/j.memsci.2005.12.017.
[29] S.A.M. Marzouk, M.H. Al-Marzouqi, M. Teramoto, N. Abdullatif, Z.M. Ismail, Simultaneous removal of CO2 and H2S from pressurized CO2–H2S–CH4 gas mixture using hollow fiber membrane contactors, Sep. Purif. Technol. 86 (2012) 88–97. doi:10.1016/j.seppur.2011.10.024.
[30] V. Fougerit, V. Pozzobon, D. Pareau, M.-A. Théoleyre, M. Stambouli, Gas-liquid absorption in industrial cross-flow membrane contactors: Experimental and numerical investigation of the influence of transmembrane pressure on partial wetting, Chem. Eng. Sci. 170 (2017) 561–573. doi:10.1016/j.ces.2017.03.042.
[31] J.-G. Lu, Y.-F. Zheng, M.-D. Cheng, Wetting mechanism in mass transfer process of hydrophobic membrane gas absorption, J. Membr. Sci. 308 (2008) 180–190. doi:10.1016/j.memsci.2007.09.051.
[32] S. Boributh, W. Rongwong, S. Assabumrungrat, N. Laosiripojana, R. Jiraratananon, Mathematical modeling and cascade design of hollow fiber membrane contactor for CO2 absorption by monoethanolamine, J. Membr. Sci. 401–402 (2012) 175–189. doi:10.1016/j.memsci.2012.01.048.
[33] V.Y. Dindore, D.W.F. Brilman, G.F. Versteeg, Modelling of cross-flow membrane contactors: physical mass transfer processes, J. Membr. Sci. 251 (2005) 209–222. doi:10.1016/j.memsci.2004.11.017.
[34] H. Kreulen, C.A. Smolders, G.F. Versteeg, W.P.M. van Swaaij, Microporous hollow fibre membrane modules as gas-liquid contactors Part 2. Mass transfer with chemical reaction, J. Membr. Sci. 78 (1993) 217–238. doi:10.1016/0376-7388(93)80002-F.

[35] K. Li, D. Wang, C.C. Koe, W.K. Teo, Use of asymmetric hollow fibre modules for elimination of H2S from gas streams via a membrane absorption method, Chem. Eng. Sci. 53 (1998) 1111–1119. doi:10.1016/S0009-2509(97)00343-6.
[36] Y. Qin, J.M. Cabral, others, Lumen mass transfer in hollow-fiber membrane processes with constant external resistances, AIChE J.-Am. Inst. Chem. Eng. 43 (1997) 1975–1987.
[37] N. Goyal, S. Suman, S.K. Gupta, Mathematical modeling of CO2 separation from gaseous-mixture using a Hollow-Fiber Membrane Module: Physical mechanism and influence of partial-wetting, J. Membr. Sci. 474 (2015) 64–82. doi:10.1016/j.memsci.2014.09.036.
[38] Y. Yan, Z. Zhang, L. Zhang, Y. Chen, Q. Tang, Dynamic Modeling of Biogas Upgrading in Hollow Fiber Membrane Contactors, Energy Fuels. 28 (2014) 5745–5755. doi:10.1021/ef501435q.
[39] A. Malek, K. Li, W.K. Teo, Modeling of Microporous Hollow Fiber Membrane Modules Operated under Partially Wetted Conditions, Ind. Eng. Chem. Res. 36 (1997) 784–793. doi:10.1021/ie960529y.
[40] G. Pantoleontos, S.P. Kaldis, D. Koutsonikolas, G. Skodras, G.P. Sakellaropoulos, Analytical and Numerical Solutions of the Mass Continuity Equation in the Lumen Side of a Hollow-Fiber Membrane Contactor with Linear or Nonlinear Boundary Conditions, Chem. Eng. Commun. 197 (2010) 709–732. doi:10.1080/00986440903288039.
[41] G. Pantoleontos, T. Theodoridis, M. Mavroudi, E.S. Kikkinides, D. Koutsonikolas, S.P. Kaldis, A.E. Pagana, Modelling, simulation, and membrane wetting estimation in gas-liquid contacting processes, Can. J. Chem. Eng. 95 (2017) 1352–1363. doi:10.1002/cjce.22790.
[42] E. Chabanon, D. Roizard, E. Favre, Modeling strategies of membrane contactors for post-combustion carbon capture: A critical comparative study, Chem. Eng. Sci. 87 (2013) 393–407. doi:10.1016/j.ces.2012.09.011.
[43] K.A. Hoff, H.F. Svendsen, Membrane contactors for CO2 absorption – Application, modeling and mass transfer effects, Chem. Eng. Sci. 116 (2014) 331–341. doi:10.1016/j.ces.2014.05.001.
[44] D. Albarracin Zaidiza, B. Belaissaoui, S. Rode, T. Neveux, C. Makhloufi, C. Castel, D. Roizard, E. Favre, Adiabatic modelling of CO2 capture by amine solvents using membrane contactors, J. Membr. Sci. 493 (2015) 106–119. doi:10.1016/j.memsci.2015.06.015.
[45] V.I. Roldugin, A.A. Shutova, A.V. Volkov, E.L.V. Goetheer, V.V. Volkov, Kinetics of carbon dioxide removal from water in flat membrane contactor, Pet. Chem. 54 (2014) 507–514. doi:10.1134/S0965544114070111.
[46] V. Fougerit, Développement d'un procédé innovant d'épuration du biogaz par mise en oeuvre de contacteurs à membranes, Université Paris-Saclay, 2017. http://www.theses.fr/2017SACLC053/document.
[47] Y. Lv, X. Yu, S.-T. Tu, J. Yan, E. Dahlquist, Wetting of polypropylene hollow fiber membrane contactors, J. Membr. Sci. 362 (2010) 444–452. doi:10.1016/j.memsci.2010.06.067.
[48] A. Dupuy, Stabilisation de l'inerface liquide-liquide dans un contacteur membranaire : application à l'extraction sélective de terpènes oxygénés d'huiles essentielles d'agrumes, AgroParisTech, 2010.
[49] A. Sengupta, P.A. Peterson, B.D. Miller, J. Schneider, C.W. Fulk Jr, Large-scale application of membrane contactors for gas transfer from or to ultrapure water, Sep. Purif. Technol. 14 (1998) 189–200.
[50] R. Sander, Compilation of Henry's law constants, version 3.99, Atmospheric Chem. Phys. Discuss. 14 (2014) 29615–30521. doi:10.5194/acpd-14-29615-2014.
[51] H. Kreulen, C.A. Smolders, G.F. Versteeg, W.P.M. van Swaaij, Microporous hollow fibre membrane modules as gas-liquid contactors. Part 1. Physical mass transfer processes: A specific application: Mass transfer in highly viscous liquids, J. Membr. Sci. 78 (1993) 197–216. doi:10.1016/0376-7388(93)80001-E.
[52] J. Xu, R. Li, L. Wang, J. Li, X. Sun, Removal of benzene from nitrogen by using polypropylene hollow fiber gas–liquid membrane contactor, Sep. Purif. Technol. 68 (2009) 75–82. doi:10.1016/j.seppur.2009.04.010.

[53] Y.-T. Zhang, X.-G. Dai, G.-H. Xu, L. Zhang, H.-Q. Zhang, J.-D. Liu, H.-L. Chen, Modeling of CO2 mass transport across a hollow fiber membrane reactor filled with immobilized enzyme, AIChE J. 58 (2012) 2069–2077. doi:10.1002/aic.12732.
[54] W. Kast, C.-R. Hohenthanner, Mass transfer within the gas-phase of porous media, Int. J. Heat Mass Transf. 43 (2000) 807–823. doi:10.1016/S0017-9310(99)00158-1.
[55] R.B. Bird, W.E. Stewart, E. Lightfoot, Transport Phenomena, 2nd edition, John Wiley & Sons, Inc., 2002.
[56] J.O. Hirschfelde, C.F. Curtiss, R.B. Bird, Molecular theory of gases and liquids, J. Polym. Sci. 17 (1954) 116–116. doi:10.1002/pol.1955.120178311.
[57] A.L. Magalhães, P.F. Lito, F.A. Da Silva, C.M. Silva, Simple and accurate correlations for diffusion coefficients of solutes in liquids and supercritical fluids over wide ranges of temperature and density, J. Supercrit. Fluids. 76 (2013) 94–114. doi:10.1016/j.supflu.2013.02.002.
[58] C.H. Hsu, H.M. Li, Viscosity of aqueous blended amines, J. Chem. Eng. Data. 42 (1997) 714–720.
[59] E.N. Fuller, P.D. Schettler, J.C. Giddings, New method for prediction of binary gas-phase diffusion coefficients, Ind. Eng. Chem. 58 (1966) 18–27.
[60] M.-C. Yang, E.L. Cussler, Designing hollow-fiber contactors, AIChE J. 32 (1986) 1910–1916.
[61] J.L. Pérez-Díaz, M.A. Álvarez-Valenzuela, J.C. García-Prada, The effect of the partial pressure of water vapor on the surface tension of the liquid water–air interface, J. Colloid Interface Sci. 381 (2012) 180–182. doi:10.1016/j.jcis.2012.05.034.
[62] R.C. Reid, J.M. Prausnitz, B.E. Poling, The Properties of Gases and Liquids, 4th edition, McGraw-Hill Inc., New York, 1987.